

Polylogarithmic-Depth Quantum Algorithm for Simulating the Extended Hubbard Model on a Two-Dimensional Lattice Using the Fast Multipole Method

Yu Wang ,  Martina Nibbi ,  Maxine Luo ,  Isabel Nha Minh Le ,  Yanbin Chen ,  J. Ignacio Cirac ,  and Christian B. Mendl , 

¹ Technical University of Munich, CIT, Department of Computer Science, Boltzmannstraße 3, 85748 Garching, Germany

² Munich Center for Quantum Science and Technology, Schellingstraße 4, 80799 München, Germany

³ Max-Planck-Institute für Quantenoptik, Hans-Kopfermann-Straße 1, 85748 Garching, Germany

⁴ Technical University of Munich, Institute for Advanced Study, Lichtenbergstraße 2a, 85748 Garching, Germany

(Dated: December 5, 2025)

The extended Hubbard model on a two-dimensional lattice captures key physical phenomena, but is challenging to simulate due to the presence of long-range interactions. In this work, we present an efficient quantum algorithm for simulating the time evolution of this model. Our approach, inspired by the fast multipole method, approximates pairwise interactions by interactions between hierarchical levels of coarse-graining boxes. We discuss how to leverage recent advances in two-dimensional neutral atom quantum computing, supporting non-local operations such as long-range gates and shuttling. The resulting circuit depth for a single Trotter step scales polylogarithmically with system size.

I. INTRODUCTION

Quantum simulation of strongly correlated electronic structure and condensed matter problems is a central and natural application of quantum computing due to the shared quantum mechanical description, and potentially offers an exponential computational advantage compared to classical methods [1–9].

Here, we focus on simulating the extended Fermi-Hubbard model [10, 11] with long-range (Coulomb) interactions on a two-dimensional (2D) lattice:

$$H = \underbrace{t \sum_{\substack{\langle a,b \rangle \\ \sigma}} \hat{c}_{a,\sigma}^\dagger \hat{c}_{b,\sigma}}_T + \underbrace{V_0 \sum_i \hat{n}_{a\uparrow} \hat{n}_{a\downarrow}}_{V_{\text{os}}} + \underbrace{\frac{1}{2} \sum_{\substack{a \neq b \\ \sigma, \sigma'}} V_{ab} \hat{n}_{a\sigma} \hat{n}_{b\sigma'}}_{V_C}, \quad (1)$$

where a, b enumerate the lattice sites and $\sigma, \sigma' \in \{\downarrow, \uparrow\}$ denote the spins. The nearest-neighbor hopping is described by T , where $\hat{c}_{a,\sigma}^\dagger$ and $\hat{c}_{a,\sigma}$ are fermionic creation and annihilation operators. V_{os} models the on-site interaction, with $\hat{n}_{a,\sigma}$ denoting the number operator, and the long-range (Coulomb) interaction is captured by V_C . Such a model plays a crucial role in investigating a variety of physical phenomena, including high-temperature superconductivity [12] and Mott insulator-metal transitions [13, 14]. Moreover, it can be specialized for chemical systems, resulting in the Pariser-Parr-Pople (PPP) model [15–17], which is widely applied to π -conjugated molecular systems, such as polyenes and aromatic hydrocarbons.

When simulating the time evolution of Eq. (1) on a quantum computer, V_{os} can be implemented using single-qubit gates in parallel. Moreover, it is well known that

the hopping term T on a 2D lattice can be realized with constant quantum circuit depth for a single Trotter step by employing local encoding methods, such as the Verstraete-Cirac encoding [18], the Bravyi-Kitaev superfast encoding [19], and compact encoding [20, 21]. In contrast, simulating V_C with all-to-all interaction is harder; when employing the fermionic SWAP network method [22] or assuming all-to-all connectivity, the depth per Trotter step remains $\mathcal{O}(N)$, where N is the number of lattice sites, and this scaling is conjectured to be optimal for generic V_{ab} coefficients. Ameliorating the cost is possible when V_C follows a power-law interaction $\propto 1/r^\mu$ ($\mu = 1$ in our case): namely, the interaction range can be truncated such that pairs $\{a, b\}$ separated by a distance r greater than ξ are neglected, with the truncation error chosen to be comparable to the Trotter error. Hence, the circuit depth can be further reduced to $\mathcal{O}(\xi^2)$ as there are $\mathcal{O}(\xi^2)$ terms per site. It has been proven that the value of ξ can be chosen small for rapidly decaying interactions (large μ) [23, 24], but still needs to be kept large for slowly decaying interactions (small μ) to maintain the desired accuracy. In the latter case, $\mathcal{O}(\xi^2)$ would not significantly improve on the expensive $\mathcal{O}(N)$ scaling.

In this work, we introduce Q2FMM, an algorithm for simulating the time evolution of the second-quantized Fermi-Hubbard model which employs the *fast multipole method (FMM)* [25–28] together with standard quantum arithmetic circuits [29–36]. Specifically, Q2FMM targets an efficient implementation of the Coulomb potential. We also discuss how the COPY operation and unbounded fan-out gates [37] can further improve overall efficiency. While the Q2FMM framework is general, we illustrate its performance using a 2D neutral-atom quantum computer [38–49], which supports long-range entangling gates and hardware operations such as atom shuttling [41–45]. In this setting, Q2FMM implements the time evolution of the long-range Coulomb term V_C with polylogarithmic circuit depth per Trotter

* 18yu.wang@tum.de

step, $\tilde{\mathcal{O}}(\log(N))$. Here, the $\tilde{\mathcal{O}}$ notation indicates that additional polylogarithmic factors in the total electron number Q are not explicitly reported. Consequently, the depth for simulating a single Trotter step of the full extended Hubbard model exhibits the same favorable scaling.

II. Q2FMM USING THE 0th-ORDER FMM

In this section, we first review the simplest variant of Q2FMM, referred to as the 0th-order Q2FMM. A more advanced formulation is presented in Sec. III. For simplicity, we neglect the spin, which will be reconsidered in Appendix A. In this case, each site can only contain at most one fermion. Furthermore, in this work, we specifically consider the Coulomb interaction described by the kernel

$$K_C(\mathbf{r}_a, \mathbf{r}_b) := 1/|\mathbf{r}_a - \mathbf{r}_b|, \quad (2)$$

where \mathbf{r}_a and \mathbf{r}_b denote the position of site a and b , respectively. More generally, the FMM is applicable to a broad class of kernels, including Yukawa [50], Helmholtz [51–53], Stokes flow [54], linear elasticity [55, 56], polyharmonic [57], and Riesz potentials [58]. Consequently, our Q2FMM implementation can potentially be extended to these models as well.

The FMM method for the Coulomb kernel given in Eq. (2) is based on its multipole expansion [59]. We employ the regular and irregular solid harmonics [60], defined as

$$R_{\ell m}(\mathbf{r}) := \sqrt{(\ell - m)! (\ell + m)!} r^\ell C_{\ell m}(\theta, \phi), \quad (3a)$$

$$I_{\ell m}(\mathbf{r}) := \sqrt{(\ell - m)! (\ell + m)!} r^{-(\ell + 1)} C_{\ell m}(\theta, \phi), \quad (3b)$$

where $C_{\ell m}(\theta, \phi)$ are the Racah-normalized spherical harmonics. Using these definitions, the Coulomb kernel can be expanded by the solid harmonic addition theorem [61] as

$$K_C(\mathbf{r}_a, \mathbf{r}_b) = \sum_{\ell=0}^{\infty} \sum_{m=-\ell}^{\ell} \sum_{j=0}^{\infty} \sum_{k=-j}^j (-1)^j R_{\ell m}(\mathbf{r}_{aA}) \times I_{\ell+j, m+k}^*(\mathbf{r}_{AB}) R_{jk}(\mathbf{r}_{bB}), \quad (4)$$

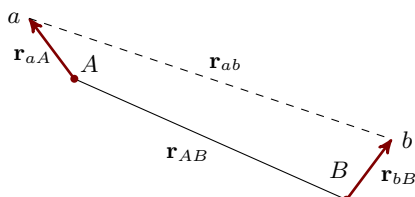


Figure 1: The expression that originally depends on the two target points a and b is rewritten in terms of local contributions around the centers A and B , together with the interaction between the two centers.

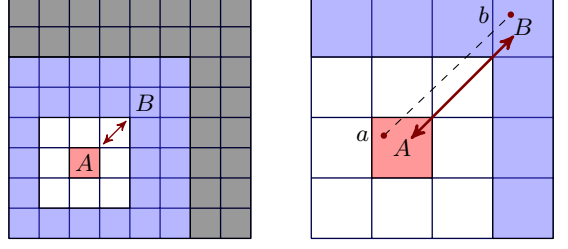


Figure 2: Blue: interaction field of the target box A , handled at the current level. White: near field for box A . The distances to A are too close to be considered at the current level and will be deferred to a finer level. Gray: far field, whose boxes have been considered at a coarser level, as shown on the right. Evaluating $K_C(\mathbf{r}_a, \mathbf{r}_b)$ is approximated by $K_C(\mathbf{r}_A, \mathbf{r}_B)$ within interaction field at each level in the 0th-order FMM.

where $I^*(\mathbf{r}_{AB})$ denotes the complex conjugate of $I(\mathbf{r}_{AB})$, and $\mathbf{r}_{AB} = \mathbf{r}_A - \mathbf{r}_B$ denotes the distance between two centers. We refer to the textbook by Helgaker et al. [59] for a detailed derivation. This formula expresses $K_C(\mathbf{r}_a, \mathbf{r}_b)$ in terms of local coordinates $\mathbf{r}_{aA} = \mathbf{r}_a - \mathbf{r}_A$ and $\mathbf{r}_{bB} = \mathbf{r}_b - \mathbf{r}_B$ relative to expansion centers A and B , as shown in Fig. 1.

To convey the core idea of our algorithm, we first present the 0th-order Q2FMM based on the 0th-order FMM, in which we constrain the expansion order to $\ell = j = 0$ in Eq. (4). However, the accuracy of 0th-order Q2FMM is limited. We discuss extensions to higher-order FMM that enable systematically improvable accuracy in Sec. III.

A. 0th-order FMM

In this subsection, we follow the introduction by L. Ying [26] to outline the 0th-order FMM. For simplicity, we focus on a square lattice, but extending to other geometries (e.g., rectangular lattices) is straightforward. In such a approximation, for two well-separated regions A and B containing points $a \in A$ and $b \in B$, the pairwise kernel $K_C(\mathbf{r}_a, \mathbf{r}_b)$ is approximated by the single representative value $K_C(\mathbf{r}_A, \mathbf{r}_B)$, where \mathbf{r}_A and \mathbf{r}_B denote the region centers (see Fig. 2). Intuitively, this exploits the uniformity of the Coulomb potential. Hence, we shift the focus from evaluating each pairwise site-site interaction to capturing the collective interaction between electron distributions in distant regions. This is a good approximation for distant, small regions. Conversely, as the regions approach each other, the approximation becomes less accurate, necessitating a reduction in the size of each region to maintain the uniformity of the Coulomb potential between the two regions.

Fig. 2 illustrates this approach using a hierarchy of boxes, which serve as “regions” above, organized in a quadtree structure. As the hierarchy is refined, each large box is subdivided into four smaller boxes, with the larger

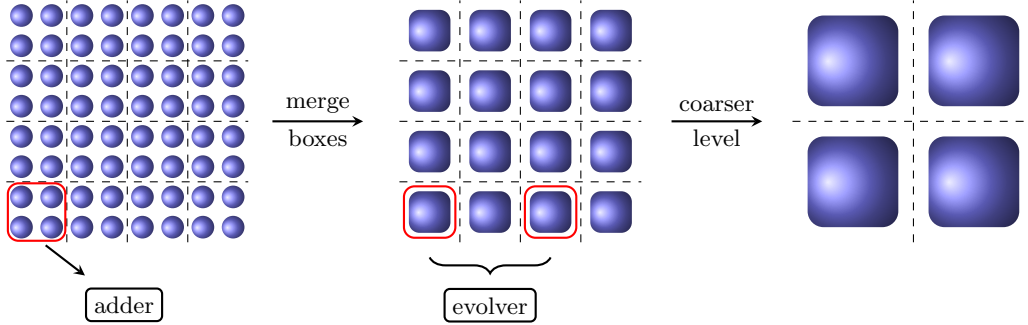


Figure 3: Illustration of the coarse-graining and time evolution algorithm. Each ball in the left diagram corresponds to a single qubit (lattice site) on the finest level. When reaching a coarser level (larger boxes), four child boxes are merged into one parent box. The time evolution phase is evaluated for all interacting pairs of boxes, displayed for one such pair in the center diagram. This procedure repeats until the coarsest level is reached. The ancilla qubits that record the occupation numbers are not drawn for visual clarity.

box referred to as the *parent box* and the smaller ones as *child boxes*. The occupation number of a parent box can be obtained by summing the occupation numbers of its child boxes. In our method, the procedure starts from the finest level. Consequently, all parent boxes at coarser levels can reuse the occupation information from previous levels. For each box, all other boxes are classified into three categories based on their distance from the current box: neighbor boxes form the *near field*, boxes not in the near field but whose parents are neighbors of the current box's parent form the *interaction list*, and the remaining ones belong to the *far field*, which is handled at coarser levels.

At each level, the summation of point-point interactions between box A and box B is approximated as:

$$V_{AB} := \frac{1}{2} \sum_{\substack{a \in A \\ b \in B}} K_C(\mathbf{r}_a, \mathbf{r}_b) \hat{n}_a \hat{n}_b \approx \frac{1}{2} K_C(\mathbf{r}_A, \mathbf{r}_B) \hat{N}_A \hat{N}_B, \quad (5)$$

where $\hat{N}_A = \sum_{a \in A} \hat{n}_a$. For each box, we only consider interactions with boxes within its interaction list that are sufficiently far away to ensure the accuracy of the approximation, while avoiding double-counting of interactions that have already been handled at coarser levels. Consequently, for each level L , which contains 4^L boxes in total, we only calculate the box-box interactions in each box A 's interaction list $I(A)$:

$$V_L := \frac{1}{2} \sum_A \sum_{B \in I(A)} K_C(\mathbf{r}_A, \mathbf{r}_B) \hat{N}_A \hat{N}_B. \quad (6)$$

Thus, we can approximate the Coulomb term as:

$$V_C = \frac{1}{2} \sum_{a \neq b} V_{ab} \hat{n}_a \hat{n}_b \approx \sum_{L=2}^{L_{\max}} V_L, \quad (7)$$

where L_{\max} denotes the finest level of the hierarchy. All interaction pairs are accounted for by systematically traversing all levels of the hierarchy in this manner.

B. Implementing 0th-order Q2FMM with quantum arithmetic circuits

Following the Trotterization technique [24, 62–65], we can approximate the time evolution of H using the second-order Trotterization as:

$$U(t) := e^{-it(T+V_{\text{os}}+V_C)} \approx \left(e^{-i\frac{\delta t}{2}(T+V_{\text{os}})} e^{-i\delta t V_C} e^{-i\frac{\delta t}{2}(T+V_{\text{os}})} \right)^d, \quad (8)$$

where d is the number of Trotter steps and $\delta t = t/d$. As discussed in Sec. I, the circuit depth for simulating the on-site and hopping terms can be reduced to $\mathcal{O}(1)$; hence, we do not elaborate on it here. In this work, we focus on the time evolution operator $e^{-i\delta t V_C}$ that corresponds to the Coulomb term, for which we employ the approximation from Eq. (7), so that

$$e^{-i\delta t V_C} \approx \prod_{L=2}^{L_{\max}} e^{-i\delta t V_L}. \quad (9)$$

By inserting Eq. (6), we get

$$e^{-i\delta t V_L} = \prod_A \prod_{B \in I_L(A)} e^{-it'_{AB} \hat{N}_A \hat{N}_B}, \quad (10)$$

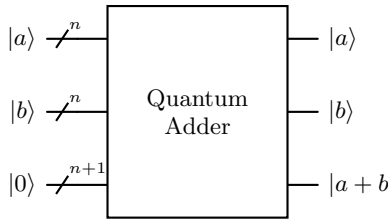
where we absorbed all the coefficients into the effective time

$$t'_{AB} = K_C(\mathbf{r}_A, \mathbf{r}_B) \delta t / 2. \quad (11)$$

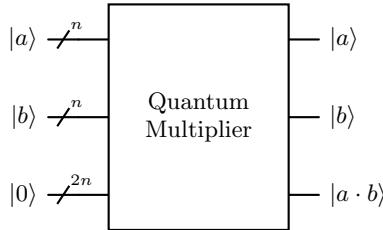
In Eq. (10), $I_L(A)$ denotes the interaction list associated with level L and the boxes with corresponding size.

The evolution of each computational basis under $e^{-i\delta t V_L}$ depends on the product $N_A N_B$, where N_A and N_B are the respective occupation numbers of box A and box B . An efficient way to simulate $e^{-i\delta t V_L}$ consists of the following steps:

1. Calculate the occupation numbers N_A and N_B for boxes A and B separately.



(a) An out-of-place quantum adder, in which the output $|a+b\rangle$ is recorded in ancilla qubits.



(b) An n -bit quantum multiplication gate. The binary representation of the result $|a \cdot b\rangle$ is stored in an ancilla register.

Figure 4: Conceptual illustration of out-of-place quantum adders and multipliers. In contrast, in-place designs overwrite the input registers with the results. The explicit circuit structure varies across different implementations.

2. Compute the product $N_A N_B$.
3. Compute the evolving phase $e^{-it'_{AB} N_A N_B}$.

At the finest level of the hierarchy, $L = L_{\max} = \log_4(N)$, the boxes coincide with the physical two-dimensional lattice. At this resolution, each lattice site corresponds to a single qubit, where $|1\rangle$ denotes an occupied site and $|0\rangle$ an empty one. Proceeding to the next level, the occupation number of each box is obtained as the arithmetic sum of the four qubits contained within it. For all coarser levels, the occupation number of a box is recursively determined by summing the occupation numbers of its child boxes, as illustrated in Fig. 3.

This summation can be carried out using a quantum adder, as exemplified in Fig. 4a. Several implementations of the quantum adder have been proposed in the literature [29–33], and in Sec. IID we will further analyze the computational complexity of this procedure and its contribution to the overall cost of the algorithm.

To approach step 2, we employ a quantum multiplier [29, 30, 34–36, 66], as exemplified in Fig. 4b. The product $N_A N_B$ is encoded as a binary string on a *product register* $|N_A N_B\rangle$ of n ancillae. For every level L , the number of ancillae n of the product register varies, as explained in Sec. IID. Finally, in step 3, the evolving phase $e^{-it'_{AB} N_A N_B}$ is implemented by applying single-qubit phase gates of the form

$$P_b = |0\rangle\langle 0| + e^{-it'_{AB} \cdot 2^b} |1\rangle\langle 1| = \begin{pmatrix} 1 & 0 \\ 0 & e^{-it'_{AB} \cdot 2^b} \end{pmatrix} \quad (12)$$

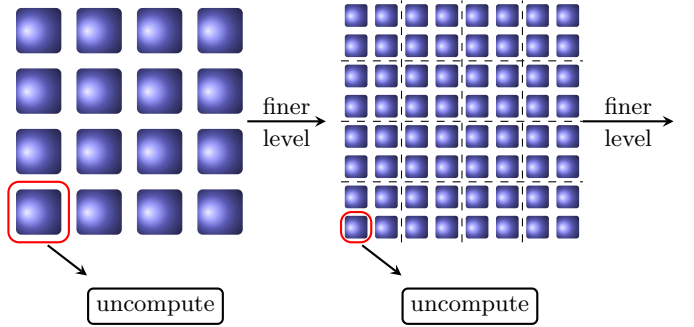


Figure 5: Uncomputing the additions in Fig. 3 “splits” the boxes by applying the inverses of the adders. This operation proceeds from the coarsest to the finest level.

to each qubit b of the product register $|N_A N_B\rangle$. The cumulative action of the gates

$$U_{AB} = \prod_{b=0}^{n-1} P_b \quad (13)$$

applies exactly the overall phase $e^{-it'_{AB} N_A N_B}$. Note that the gates P_b can be applied in parallel. The obtained phase $e^{-it'_{AB} N_A N_B}$ is first imprinted on the ancilla qubits that record the product $N_A N_B$. We must uncompute the quantum multiplier to transfer the phase back to the qubits that represent the quantum state.

To reuse already computed occupation numbers, we initiate Q2FMM from the finest level, where each box represents one lattice site. At this level, the time evolution is computed by the interaction between individual qubits that are in each other’s interaction list. For the coarser levels, the occupation number of the boxes is obtained by summing the occupation numbers of their children. To avoid the premature erasure of information stored in ancilla qubits from previous levels, we defer uncomputing until all evolving phases have been evaluated. Therefore, the full quantum circuit can be partitioned into a compute phase and an uncompute phase. In the compute phase, adapted to the 2D architecture, each level in Eq. (9) is implemented as illustrated in Fig. 3. At the finest level, where interactions are restricted to single grid points, we apply the time evolution operator directly. For the other levels, we proceed as follows:

1. We first obtain the occupation number of each box at the current level by summing the values of its four children using quantum adders.
2. Subsequently, we implement the evolution in Eq. (10) with these occupation numbers by means of the quantum multiplier.

This procedure is recursively repeated to transverse the entire hierarchy. Note that after the summation, every four child boxes are efficiently merged into their corresponding parent box, as illustrated in Fig. 3.

Since the quantum adders and multipliers are reversible, the uncomputing merely decomposes the per-box sums and leaves the accumulated phase intact, so it is safe to perform. As illustrated in Fig. 5, this operation must be applied to each box in the reverse order of their execution in the compute phase. As a concrete example, a quantum circuit for the 0th-order Q2FMM is presented in Appendix B, shown for a one-dimensional lattice for illustrational simplicity.

C. Advanced techniques for improving efficiency

In this section, we describe three techniques that significantly enhance the efficiency of Q2FMM.

1. The *COPY* operation

Since the terms in Eq. (10) commute, the corresponding phases can be evaluated simultaneously for each interaction term within a given level. Intuitively, this follows from the fact that the time evolution governed by the Coulomb operator leaves the occupation numbers unchanged, as discussed earlier. Thus, an efficient strategy for computing the phases is to first *COPY* the occupation information and then compute the evolving phase in parallel.

The *COPY* operation, also commonly known as *Transversal CNOT* [67–69] or *Element-wise CNOT* [70], is exemplified in Fig. 6. Concretely, in our case, we need to *COPY* the occupation information of each box $|I(A)|$ times, where $|I(A)| \leq 27$ due to the geometric setup. Thus, the number of required ancilla qubits scales linearly with the number of boxes. With these “copies,” the phase evolution for all interacting box pairs can be computed in parallel, after which the *COPY* operation is uncomputed to disentangle the ancilla registers. Therefore, the quantum circuit at each level effectively requires only a single round of time-evolution computation, rather than $|I(A)|$ sequential layers.

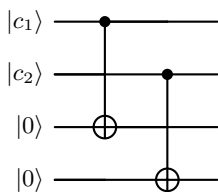


Figure 6: “Copying” occupation numbers to ancilla qubits via element-wise CNOTs, exemplified by a two-qubit state and two ancilla qubits.

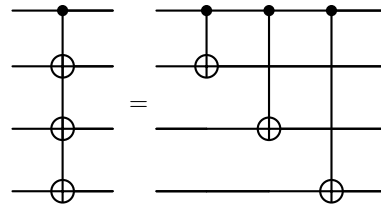


Figure 7: Definition of the fan-out gate illustrated with four qubits.

2. Bringing box information together: the *shuttling* operation

The qubits encoding the occupation information of each box (and also their copies when *COPY* is utilized) are typically located at its corresponding geometric location. To evaluate the long-range interaction between two spatially separated boxes, either (i) the hardware must support long-range quantum gates or (ii) only local gates are available, and the relevant information must be brought together. Below, we discuss the latter case in detail.

Under the constraint of nearest-neighbor connectivity, the interaction is typically implemented through a series of SWAP gates that effectively “move” the ancilla qubits of the two boxes into proximity. The circuit depth associated with these SWAP operations scales linearly with the distance r_{AB} between the boxes A and B .

Alternatively, if hardware supports qubit shuttling, i.e., physically transporting qubits between regions, one replaces a SWAP chain of depth $\mathcal{O}(r_{AB})$ by only two shuttling operations, reducing the routing depth to $\mathcal{O}(1)$. Shuttling operations, or functionally equivalent long-range coupling, have been the subject of extensive theoretical proposals and experimental realizations in multiple quantum computing platforms, such as the neutral atom quantum computer [41–45] and the trapped-ion quantum computer [71–77].

3. The unbounded fan-out gate

The unbounded fan-out gate [37], where a single qubit simultaneously controls multiple targets as illustrated in Fig. 7, can also provide significant advantages. Here, “unbounded” means we treat the fan-out operation as a constant-depth primitive, independent of the number of targets. Recent experimental progress demonstrated the realization of the fan-out gate in shallow depth [78–81], enabling further optimizations of our quantum algorithm.

It is worth noting that, without utilizing the FMM approximation, the unbounded fan-out gate can perform a single Trotter step for the long-range Coulomb term in depth $\mathcal{O}(1)$. As proven in [37], the commuting gates can be applied to the same qubits simultaneously with unbounded fan-out gates. However, this procedure needs

$\mathcal{O}(N)$ ancilla qubits per site and thus $\mathcal{O}(N^2)$ ancilla qubits in total.

To mitigate the quadratic ancilla blow-up while preserving low depth, we integrate the fan-out gate into Q2FMM, achieving a more favorable ancilla-depth trade-off. Specifically, we can employ the unbounded fan-out gate in both the **COPY** operation and the arithmetic circuits. i.e., quantum adder and multiplier. For the **COPY** operation, the fan-out gate enables us to **COPY** the occupation information of each box for $|I(A)|$ “copies” within with depth 1.

For arithmetic operations, P. Høyer and R. Špalek [37] proved that the depth of the arithmetic circuits can be reduced to $\mathcal{O}(\log^* n)$ by employing the unbounded quantum fan-out gate, where $\log^* n$ (the iterated logarithm) is the number of times the logarithm must be applied to n to reduce it to at most 1. Here, n is the operand bit length. The iterated logarithm function $\log^* n$ is a sublogarithmic function that grows very slowly with n . Even for input sizes as large as the estimated number of atoms in the observable universe, $\log^* n \leq 5$. Consequently, $\log^* n$ can be treated as a *constant* for all practical input sizes. As detailed in Sec. IID 2 and Table I, integrating the fan-out gate into the arithmetic circuits of Q2FMM yields a more balanced trade-off between ancilla-qubit usage and circuit depth.

We present the ancilla-depth trade-off with and without Q2FMM in Table I, where we allow the shuttling operation and assume it admits depth $\mathcal{O}(1)$; we discuss the detailed derivation in Sec. IID 2.

Table I: The circuit depth and overall ancilla qubits needed to carry out a single Trotter step for the Coulomb term using the unbounded fan-out gate.

Method	Circuit Depth	# Ancillae
Fan-out only	$\mathcal{O}(1)$	$\mathcal{O}(N^2)$
Q2FMM + Fan-out	$\mathcal{O}(\log N)$	$\mathcal{O}(N)$

D. Circuit depth for 0th-order Q2FMM

So far, we have introduced the basic algorithm founded on the 0th-order FMM to convey the core idea in the simplest setting. Before turning to the higher-order Q2FMM, we first analyze the circuit depth of the 0th-order scheme. This not only highlights why our algorithm achieves favorable complexity but also provides intuition for the higher-order case, whose scaling follows a similar structure.

The circuit depth achieved by Q2FMM is architecture-dependent, since it is determined by the native operations supported by each platform. In what follows, we focus on three representative cases: (i) a 2D neutral-atom quantum computer allowing shuttling, (ii) a 2D neutral-atom quantum computer further allowing unbounded fan-out gates, and (iii) a 2D architecture that only allows nearest

connectivity.

1. Depth with shuttling

Here, we take a 2D neutral-atom quantum computer [38–45] as a representative example and analyze the resulting circuit depth. In such platforms, *atom shuttling* can be implemented using optical tweezers, enabling the rearranging of the position of the atoms, which effectively allows for connectivity between distant qubits with high parallelism [42–45]. In our algorithm, we can take advantage of shuttling to bring distant qubits together for local arithmetic circuits. Furthermore, the recent advances in neutral atom quantum computing demonstrate a tweezer reload rate of 300000 atoms per second and the initialization of over 30000 qubits per second [48], underscoring the platform’s scalability and the availability of abundant temporary ancilla qubits. Although the **COPY** operation requires many qubits, the ability to rapidly prepare large qubit strings enables such **COPY** gates to be practical. This enables a high degree of parallelism by allowing multiple target pairs within a box to be evaluated concurrently, significantly reducing the circuit depth, rather than simulating each interaction term sequentially.

By exploiting atom shuttling and an efficient implementation of the **COPY** operation, the most significant contribution to the overall circuit depth arises then from the quantum arithmetic circuits, particularly from the dominant component between the quantum adder and the time evolution, which is implemented via a quantum multiplier. In this regard, Q2FMM offers substantial flexibility in choosing among different arithmetic implementations at each step. For instance, the addition or multiplication operation can be implemented using various quantum adders [29–33] or multipliers [29, 30, 34–36, 66], each offering different trade-offs between circuit depth and ancilla qubit requirements. In practice, the optimal choice depends on the characteristics of the underlying hardware platform. As a rule, we can first select a quantum multiplier, which typically dominates the computational cost, and then choose a quantum adder whose scaling remains strictly better than that of the multiplier. For simplicity, we omit a detailed discussion on the specific choice of quantum adders, as they are generally less costly.

We assume an input length of $n = \log_2(Q + 1)$, corresponding to the largest possible value in our calculation, where Q denotes the number of electrons of the system. Selecting an efficient quantum multiplier is crucial for maintaining a favorable circuit depth scaling. For instance, the depth scales as $\mathcal{O}(\log^{1.3} Q)$ per level when using the quantum multiplier proposed by Kahanamoku-Meyer et al. [66], in which no ancilla qubits are needed. Since there are $\mathcal{O}(\log(N))$ levels that we need to run the quantum arithmetic circuits in total, the overall circuit depth of the algorithm exhibits a polylogarithmic scaling, $\mathcal{O}(\log N \cdot \log^{1.3} Q)$, when the quantum multiplier of

Ref. [66] is employed. As shown in Sec. III D, Q2FMM for higher-order FMM retains a similar favorable depth scaling. We summarize the total circuit depth of the 0th-order Q2FMM under different hardware capacities in Table II.

2. Depth with the unbounded fan-out gate

As a further improvement, the fan-out gate can be employed to efficiently implement the quantum arithmetic circuits in Q2FMM. As discussed in Sec. II C 3, the depth of both the quantum adder and multiplier is reduced to $\mathcal{O}(\log^* n)$. Considering the input length $n = \log_2(Q+1)$, this corresponds to a depth of $\mathcal{O}(\log^* \log Q)$. Since the algorithm involves $\log_4 N$ hierarchical levels, the overall circuit depth scales as $\mathcal{O}(\log N \cdot \log^* \log Q)$, which can be further simplified to $\mathcal{O}(\log N)$, as the iterated logarithm can be regarded as a constant.

Since a fan-out-based quantum multiplier requires $\mathcal{O}(n^2)$ ancilla qubits, whereas a quantum adder needs only $\mathcal{O}(n)$ [37], the total ancilla requirement for employing fan-out-based arithmetic circuits can be estimated as follows. Because the ancilla qubits used in the arithmetic circuits can be recycled across coarser levels, the overall demand is determined by the peak usage among all levels. At level l , where each box contains 4^l grid points, the lattice is partitioned into 4^{L-l} boxes, and each box requires at most $\mathcal{O}(\log_2^2(4^l + 1))$ ancilla qubits for the multiplier. Consequently, the total ancilla count scales as $\mathcal{O}((N/\beta) \log_2^2(\beta + 1))$. With $\beta \in \{1, \dots, 4^L\}$, this expression attains its maximum at $\beta = 4$, yielding an overall $\mathcal{O}(N)$ ancilla requirement.

Therefore, the fan-out gate not only accelerates Q2FMM, but Q2FMM in turn enables the fan-out-based approach to achieve a more favorable balance between ancilla qubit usage and circuit depth, as mentioned in Sec. II C 3.

3. Depth when constrained to nearest connectivity

Our algorithm remains efficient even without the shuttling or fan-out gate. When constrained to the nearest connectivity, the dominant contribution to the circuit depth arises from using SWAP gates to “move” the ancilla qubits of two boxes together. The number of required SWAP gates depends on the distance between the two target boxes, i.e., the number of sites between these two boxes. The distance ρ_L between boxes in each other’s interaction list is:

$$\rho_L = \mathcal{O}(\xi_{\max}/2^L), \quad (14)$$

where ξ_{\max} is the linear size of the 2D lattice, i.e., $\xi_{\max}^2 = N$. Therefore, the total depth of executing SWAP gates

across all levels scales as

$$\sum_{L=2}^{L_{\max}-1} \mathcal{O}(\xi_{\max}/2^L) = \mathcal{O}(\xi_{\max}) = \mathcal{O}(\sqrt{N}). \quad (15)$$

Asymptotically, \sqrt{N} grows faster than the polylogarithmic depth of the quantum arithmetic circuits. Thus, the overall circuit depth for simulating a single Trotter step is $\mathcal{O}(\sqrt{N})$, without the use of long-range gates or shuttling. This depth scaling outperforms the $\mathcal{O}(N)$ depth required by the fermionic SWAP network [22].

4. Error analysis

In the context of error analysis, the total error originates from two main sources: Trotterization and the FMM approximation. Although the 0th-order FMM is relatively inaccurate [26], its accuracy can be improved by tightening the acceptance criterion, i.e., increasing the minimum separation required for interaction pairs. Furthermore, the approximation error decreases geometrically with increasing expansion order p , and we discuss these in detail in Sec. III D.

III. Q2FMM FOR HIGHER-ORDER FMM

In this section, we extend Q2FMM to higher-order FMM, which is essential for achieving better accuracy. The resulting quantum circuit retains a structure similar to that of the 0th-order case.

A. Higher-order FMM formulas

Assuming two well-separated boxes A and B , the box-box interaction in the higher-order FMM can be calculated by summing up all the interaction pairs as given in Eq. (4):

$$\sum_{a \in A} \sum_{b \in B} \left| \frac{q_a q_b}{\mathbf{r}_a - \mathbf{r}_b} \right| \approx \sum_{\ell=0}^p \sum_{m=-\ell}^{\ell} \sum_{j=0}^{p-\ell} \sum_{k=-j}^j \left(\sum_{a \in A} R_{\ell m}(\mathbf{r}_{aA}) q_a \right) \times I_{\ell+j, m+k}(\mathbf{r}_{AB}) \left(\sum_{b \in B} R_{jk}(\mathbf{r}_{bB}) q_b \right) (-1)^j. \quad (16)$$

The infinite series over ℓ and j in Eq. (4) is truncated such that $\ell + j \leq p$, where p denotes the FMM truncation order, controlling the trade-off between accuracy and computational cost. Here, $q_a \in \{0, 1\}$ represents the electron number at point a . Assuming that each box contains κ grid points, Eq. (16) reduces the computational effort from evaluating all κ^2 point-to-point interactions to only $\mathcal{O}(\kappa(p+1)^2)$ local terms, as shown in Fig. 8. Note that the case $p=0$ corresponds exactly to the 0th-order

FMM discussed in Sec. II. The expansion converges for well-separated boxes, i.e.,

$$\max\{\|\mathbf{r}_{aA}\|, \|\mathbf{r}_{bB}\|\} < \|\mathbf{r}_{AB}\|, \quad (17)$$

and the interaction-list criterion in our hierarchical structure automatically satisfies this condition. Incorporating Eq. (16) into the hierarchical framework discussed in Sec. II yields the higher-order Q2FMM, in which box-box interactions are evaluated using Eq. (16).

The overall procedure is analogous to the 0th-order case: we first evaluate the energy on the second finest level, where each box contains only four grid points. From there, the energies of coarser levels are aggregated. At each level, we compute box-box interactions, perform the time-evolution, and then proceed to the next coarser level, traversing the hierarchy from finest to coarsest. Techniques such as the COPY operation can be seamlessly incorporated into the higher-order formulation as well. What differs from the 0th-order scheme is the specific formulation of the interaction evaluation and the mechanism by which each coarser level reuses information computed on the finer levels, as discussed in Sec. III C.

B. Implementation of higher-order FMM on a quantum computer

Replacing $q_a \mapsto \hat{n}_a$ in Eq. (16) defines the interaction operator V_{AB} , which consists solely of products of number operators, as in the 0th-order case. Consequently, any configuration $|c_{AB}\rangle$ (i.e., computational basis state of box A and B) is an eigenstate of V_{AB} :

$$V_{AB} |c_{AB}\rangle = E_{AB}^c |c_{AB}\rangle, \quad (18)$$

where E_{AB}^c denotes the corresponding eigenvalue computed via Eq. (16). The time evolution governed by V_{AB} therefore results only in phase changes for each configuration $|c_{AB}\rangle$:

$$e^{-itV_{AB}} |c_{AB}\rangle = e^{-itE_{AB}^c} |c_{AB}\rangle. \quad (19)$$

Hence, our task reduces to evaluating the Coulomb potential between A and B for each configuration using Eq. (16) and generating the corresponding evolving phase through single-qubit projector gates, as discussed in Eq. (12) for the 0th-order case.

As discussed for the 0th-order FMM in Sec. II, box-box interactions at each level are obtained from calculations performed on the immediately finer level. To illustrate this procedure, we begin with the second finest level, where each box contains four grid points of the physical Fermi-Hubbard lattice, and consequently discuss how the computed information propagates to coarser levels. We first simplify Eq. (16) by defining the multipole expansion $M_{\ell m}^A$ and M_{jk}^B :

$$M_{\ell m}^A := \sum_{a \in A} R_{\ell m}(\mathbf{r}_{aA}) q_a, \quad (20a)$$

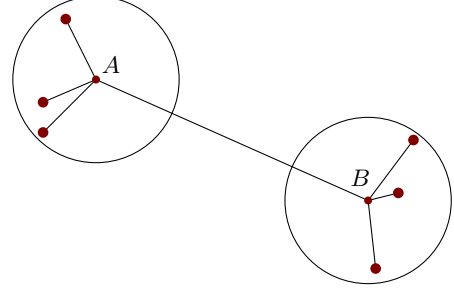


Figure 8: Illustration of higher-order FMM, Eq. (16): The overall pairwise sum is obtained by first calculating per-box local information and then evaluating box-box interactions.

$$M_{jk}^B := \sum_{b \in B} R_{\ell m}(\mathbf{r}_{bB}) q_b, \quad (20b)$$

so that Eq. (16) can be rewritten as:

$$E_{AB} = \sum_{a \in A} \sum_{b \in B} \left| \frac{q_a q_b}{\mathbf{r}_a - \mathbf{r}_b} \right| \approx \sum_{\ell=0}^p \sum_{m=-\ell}^{\ell} \sum_{j=0}^{p-\ell} \sum_{k=-j}^j M_{\ell m}^A \times I_{\ell+j, m+k}^*(\mathbf{r}_{AB}) M_{jk}^B (-1)^j. \quad (21)$$

An efficient way to compute $M_{\ell m}^A$ and M_{jk}^B in Eq. (20) is to encode the binary representation of $R_{\ell m}(\mathbf{r}_{aA})$, classically precomputed by Eq. (3a), as a sequence of CNOT gates conditioned on $|q_a\rangle$. As illustrated in Fig. 9, if the register storing the result of $R_{\ell m}(\mathbf{r}_{aA}) q_a$ is initialized to $|00\cdots 0\rangle$, applying these CNOT gates yields the final state that correctly encodes the product $R_{\ell m}(\mathbf{r}_{aA}) q_a$. Because computational basis states natively encode integers, we use fixed-point scaling for non-integer values; for example, for a decimal $b_1 b_2 b_3 b_4$, we store $b_1 b_2 b_3 b_4$ and carry a scale factor 10^{-2} ; equivalently, the extra factor 10^{-2} is absorbed into the time duration during the time evolution step. The quantity $M_{\ell m}^A$ is then obtained by accumulating the $R_{\ell m}(\mathbf{r}_{aA}) q_a$ terms using quantum adders. After obtaining $M_{\ell m}^A$ and M_{jk}^B , the evaluation of E_{AB} in Eq. (21) becomes straightforward: each term in the sum is computed with quantum multiplication and accumulated with quantum addition. Similar to the 0th-order Q2FMM, the resulting time evolution phase is obtained by applying the phase gates as defined in Eq. (13). Note that, for a fixed FMM order p , the depth of this stage is independent of the system size N .

C. Translation of multipole expansions

So far, we have only discussed how to calculate the time evolution for the second finest level, where each box contains four grid points. Similar to the 0th-order Q2FMM discussed in Sec. II, computations for coarser levels can leverage information from the child boxes. For the higher-order case, the parent box's multipole expansion is obtained by applying a multipole-to-multipole

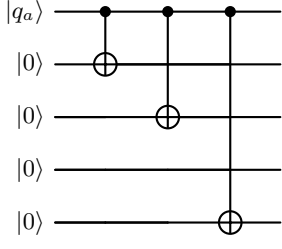


Figure 9: Computation of $R_{\ell m}(\mathbf{r}_{aA})q_a$ using CNOT gates, illustrated for the case where $R_{\ell m}(\mathbf{r}_{aA})$ is encoded in the integer form $|1101\rangle$. A CNOT gate is applied to each qubit corresponding to a nonzero bit of $R_{\ell m}$. When $q_a = 0$, the output state is $|0000\rangle$; when $q_a = 1$, the output state is $|1101\rangle$, both of these two cases correctly encoding the product $R_{\ell m}q_a$. Note that we might need more qubits to reach the desired precision.

(M2M) translation to each child. In other words, the child box’s multipole expansion $M_{\ell m}$ can be reused by shifting its expansion origin from the child’s center to the parent’s center. The parent box’s multipole expansion is then obtained by summing the shifted expansions from all child boxes. For example, let \mathbf{x}_C and \mathbf{x}_P be the centers of a child C and its parent P , respectively, and define the displacement $\mathbf{d} := \mathbf{x}_P - \mathbf{x}_C$ (from child to parent). The translation from the multipole expansion of the child box $M_{\ell m}^C$ to the one of parent center $M_{\ell m}^{C \rightarrow P}$ can be obtained by the addition theorem [59]:

$$M_{\ell m}^{C \rightarrow P} = \sum_{j=0}^{\ell} \sum_{k=-j}^j R_{\ell-j, m-k}(-\mathbf{d}) M_{jk}^C. \quad (22)$$

A parent’s total multipole expansions are then obtained by summation over all its child boxes’ contributions:

$$M_{\ell m}^P = \sum_C M_{\ell m}^{C \rightarrow P}. \quad (23)$$

This process is repeated at each coarser level. The Coulomb interaction between parent boxes is then computed from their multipole expansions as given in Eq. (21). Similar to the 0th-order Q2FMM, uncomputing is needed to transfer the accumulated phases back to the qubits. In practice, we defer the uncomputing so that the computed multipole expansions can be reused at the next coarser level, just as in the 0th-order scheme.

D. Circuit depth and error analysis

Following the outline presented in Sec. II D for 0th-order Q2FMM and likewise assuming a 2D neutral atom quantum hardware, the circuit depth for higher-order Q2FMM is similarly dominated by quantum arithmetic circuits, especially the quantum multipliers. Concretely, Eqs. (21) – (23) are implemented in a quantum device using quantum addition and quantum multiplication. Note

that Eq. (22) is local to each child box and can be executed in parallel across children. For each child, and with fixed truncation order p , executing both Eq. (21) and Eq. (22) requires $\mathcal{O}(p^4)$ multiplications. In other words, the number of multiplications is *constant* for fixed p .

The depth of the quantum multiplier used in Eq. (21) and Eq. (22) is governed by the input length, i.e., the bit length of the ancilla register that stores the multipole coefficients $M_{\ell m}^A$ for box A , which satisfy the bound:

$$\begin{aligned} |M_{\ell m}^A| &= \left| \sum_{i=1}^{Q_b} q_i R_{\ell m}(\mathbf{r}_{iA}) \right| \\ &\leq \sum_{i=1}^{Q_b} |q_i| |R_{\ell m}(\mathbf{r}_{iA})| \\ &\leq Q_b \max_{1 \leq i \leq Q_b} |R_{\ell m}(\mathbf{r}_{iA})| \\ &\leq Q_b \sqrt{(\ell - m)! (\ell + m)!} r_A^\ell, \end{aligned} \quad (24)$$

where r_A is the radius of box A (the upper bound of r_{iA}), and Q_b denotes the number of electrons in a given box. After scaling $M_{\ell m}^A$ by $\ell! r_A^\ell$, the resulting value is strictly less than Q and can be encoded as a binary fixed-point number. Hence, to represent $M_{\ell m}^A$ within binary precision ϵ , we need at most:

$$n_{\epsilon, \text{max}} = \log_2(Q + 1) + \log_2(1/\epsilon) \quad (25)$$

bits, where the first term encodes the integer range and the second term encodes the binary fractional precision.

As summarized in Table II, using the multiplier proposed by Kahanamoku-Meyer et al. [66], the circuit depth *per level* scales asymptotically as $\mathcal{O}((\log Q + \log(1/\epsilon))^{1.3})$, which is reduced to $\mathcal{O}(\log^*(\log Q + \log(\frac{1}{\epsilon})))$ if fan-out gates are available. Since there are $\log(N)$ levels in total, the total depth for simulating a single Trotter step remains *polylogarithmic*. For instance, when the quantum multiplier of Ref. [66] is selected, the overall circuit depth scales as $\mathcal{O}(\log(N) \cdot (\log Q + \log(1/\epsilon))^{1.3})$; other widely known quantum multipliers such as QFT-based [82] multiplier also help reach logarithmic depth scaling.

Similar to the analysis in Sec. II D 2, we estimate the qubit requirement for storing multipole expansions as follows. Let the number of bits required to store a single coefficient with absolute precision ϵ be

$$n_\epsilon = \log_2(\beta + 1) + \log_2(1/\epsilon), \quad (26)$$

where $\beta \in \{1, \dots, 4^L\}$ denotes the number of grid points contained in a box at a given level (so that $\beta = 1$ corresponds to the finest level). At a level with box size β , there are N/β boxes, and $M_{\ell m}$ contains $(p+1)^2$ coefficients. Hence, the total number of ancilla qubits needed at that level scales as

$$N_s \propto \frac{N}{\beta} (p+1)^2 n_\epsilon = \frac{N}{\beta} (p+1)^2 (\log_2(\beta+1) + \log_2(1/\epsilon)). \quad (27)$$

Table II: The asymptotic scaling of circuit depth and ancilla requirements to carry out a single Trotter step for the Coulomb term with the 0th-order and higher-order Q2FMM under different hardware capacity assumptions. The abbreviation “NA” denotes neutral-atom quantum computers, and all hardware configurations are assumed to be implemented on a 2D architecture. For the 0th-order case, we assume an input length of $\log_2(Q + 1)$ for the quantum adders and multipliers, whereas for the higher-order case we assume an input length $n_\epsilon = \log_2(Q + 1) + \log_2(1/\epsilon)$. The circuit depth for the NA with only shuttling is estimated using the multiplier proposed by Kahanamoku-Meyer et al. [66] as an example. The iterated logarithm related to the fan-out gate is regarded as a constant. Although the **COPY** operation reduces the circuit depth, it does not affect the asymptotic depth scaling, so the **COPY** operation is not included here. Both the spinless and spinful cases of Q2FMM share the same asymptotic scaling.

Q2FMM	Error	Hardware Capacity	Circuit Depth	Shuttling Depth	# Ancillae
0 th -order	$\mathcal{O}(r/R)$	NA with shuttling	$\mathcal{O}(\log N \cdot \log^{1.3} Q)$	$\mathcal{O}(\log N)$	
		NA with shuttling & Fan-out	$\mathcal{O}(\log N)$	$\mathcal{O}(\log N)$	$\mathcal{O}(N)$
		Only Nearest connectivity	$\mathcal{O}(\sqrt{N})$	N/A	
p th -order	$\mathcal{O}(r/R)^{p+1}$	NA with shuttling	$\mathcal{O}(\log N \cdot (\log Q + \log(1/\epsilon))^{1.3})$	$\mathcal{O}(\log N)$	
		NA with shuttling & Fan-out	$\mathcal{O}(\log N)$	$\mathcal{O}(\log N)$	$\mathcal{O}(N)$
		Only Nearest connectivity	$\mathcal{O}(\sqrt{N})$	N/A	

Even under a large error tolerance $\epsilon \leq 10^{-3}$ to represent a decimal, a direct maximization shows that N_s is largest at the finest level $\beta = 1$. In this case, $n_\epsilon = 1 + \log_2(1/\epsilon)$, so storing all $(p+1)^2$ terms in $M_{\ell m}$ for one site requires $(p+1)^2(1 + \log_2(1/\epsilon))$ qubits. Hence, for fixed p and ϵ , the per-site ancilla cost of storing the multipole expansion is *constant*, and the total number of ancilla qubits scales with the number of sites N . We summarize the comparison of circuit depth and ancilla requirements for the 0th-order and higher-order Q2FMM under various hardware assumptions in Table. II.

For an arbitrary state $|\psi\rangle = \sum_i \alpha_i |i\rangle$, the higher-order Q2FMM introduces an error ϵ_F^i to the overall Coulomb interaction for a given Fock basis state $|i\rangle$. When computing the time evolution governed by the Coulomb interaction, such an energy error leads to the time evolution error of basis state $|i\rangle$:

$$\begin{aligned} \left| e^{-i\delta t(E_C^i + \epsilon_F^i)} - e^{-i\delta t E_C^i} \right| &= \left| e^{-i\delta t E_C^i} \right| \left| e^{-i\delta t \epsilon_F^i} - 1 \right| \\ &= \left| e^{-i\delta t \epsilon_F^i} - 1 \right| \\ &\leq \delta t |\epsilon_F^i| \end{aligned} \quad (28)$$

with a small δt , where we denote the overall Coulomb interaction of $|i\rangle$ by E_C^i . Therefore, the overall time evolution error incurred by Q2FMM for an arbitrary state $|\psi\rangle = \sum_i \alpha_i |i\rangle$ is bounded by:

$$\epsilon_{\delta t} \leq \sum_i |\alpha_i|^2 |\epsilon_F^i| \delta t. \quad (29)$$

The FMM errors ϵ_F^i scales as $\mathcal{O}(\frac{r}{R})^{p+1}$ [27, 59], where R denotes the center-center distance between interacting boxes and r the box radius at a given level. Hence, the time evolution error scales as:

$$\epsilon_{\delta t} \sim \mathcal{O}\left(\delta t \left(\frac{r}{R}\right)^{p+1}\right) \quad (30)$$

for a single time evolution step with duration δt . Importantly, this error decreases rapidly with increasing expansion order p , exhibiting geometric convergence.

IV. CONCLUSION AND DISCUSSION

In this work, we present a quantum algorithm with polylogarithmic depth for simulating the extended Hubbard model. This algorithm builds upon the FMM, which reformulates the computation of pairwise interactions into inter-box interactions, thereby reducing the overall computational complexity. Furthermore, Q2FMM leverages recent advances in 2D neutral-atom quantum computing platforms, where long-range gates and shuttling are experimentally supported. It is worth emphasizing that, although we describe Q2FMM within the FMM framework, the workflow is not strictly FMM. Rather, it is more appropriately viewed as a multipole expansion algorithm with a hierarchical structure, which is inspired by FMM.

Q2FMM is not limited to the extended Hubbard model; it is also potentially applicable to ab initio molecular Hamiltonians discretized on real-space grids, as discussed in Appendix C. Extending the algorithm to this setting would profit from a corresponding three-dimensional quantum hardware topology layout, which might become available in the future. Additionally, the truncation of the power-law interaction (which decays with distance) can also be incorporated into Q2FMM. The number of levels can be reduced by terminating Q2FMM at a level where the distance between boxes exceeds the chosen truncation distance ξ . This yields a total number of levels $\mathcal{O}(\log \xi)$ to be executed.

We have noticed that a recent work by D. W. Berry et al. [83] also utilizes the FMM for quantum simulation in the context of quantum chemistry. The authors employ a real-space first-quantized representation of the molecular Hamiltonian, whereas our work is based on a second-quantized formulation. It would be of particular interest to extend their framework to the 2D extended Hubbard model and compare its performance directly with that of Q2FMM.

ACKNOWLEDGMENTS

This research is part of the Munich Quantum Valley, which is supported by the Bavarian State Government with funds from the Hightech Agenda Bayern Plus. We also thank the Munich Center for Quantum Science and Technology. The packages `quantikz` [84] and `yquant` [85] were used for drawing the quantum circuit diagrams.

Appendix A: Generalization to the spinful Fermi-Hubbard model

Restoring the spin allows each site to host up to two fermions (one per spin), and only slightly modifies the long-range term:

$$V_C = \sum_{a \neq b} V_{ab} \hat{n}_a \hat{n}_b, \quad (\text{A1})$$

where we rewrite the number operators as

$$\hat{n}_a = \sum_{\sigma \in \{\uparrow, \downarrow\}} \hat{n}_{a\sigma}, \quad \hat{n}_{a\sigma} = \hat{c}_{a\sigma}^\dagger \hat{c}_{a\sigma}. \quad (\text{A2})$$

Adapted to Q2FMM, each site i is now encoded by *two* adjacent physical qubits. The only change to the circuit appears at the second finest level $L = \log_4(N) - 1$, where each site's information is propagated to their parent boxes. Here, we simply apply the method illustrated in Fig. 9 to account for the contributions from the *two* qubits representing a site. Consequently, at the finest level, there are eight qubits (corresponding to four sites) that are merged into their parent box. Accordingly, we require one additional ancilla qubit to store the information for each box.

Appendix B: Overall quantum circuit exemplified by a one-dimensional lattice

We illustrate the structure of the 0th-order Q2FMM in Fig. 11. For visual clarity, the circuit corresponds to a one-dimensional (1D) lattice with 16 sites, as shown in Fig. 10, and ignores spin degrees of freedom. The overall quantum circuit for a single Trotter step is composed of three main components: the time evolution $e^{-it(T+V_{\text{os}})}$ for the hopping term T and the on-site term V_{os} , the compute phase, and the uncompute phase, which are separated by red slices in Fig. 11. A detailed description of the compute and uncompute phases, which aim to evaluate the time evolution governed by the long-range Coulomb term, is provided in Sec. II B.



Figure 10: One-dimensional lattice geometry and hierarchy of boxes used for the circuit instantiation in Fig. 11.

The compute phase begins by evaluating the time evolution at the finest level, where only near-neighbor interactions are involved and can be implemented straightforwardly; hence, we do not detail it here. When reaching a coarser level, we employ quantum adders to “merge” the boxes (grids at the finest level), as illustrated in Sec. II B and Fig. 3 of the main text. The blue bundle lines denote the ancilla registers, which are used to store the results of quantum adders, i.e., the summation of occupation numbers. The time evolution between boxes at a given level is then evaluated by the `Evo` gate, which is displayed as non-adjacent multi-qubit gates connected by a wave line. We omit the non-participating qubits between the two halves of the `Evo` gate and place the participating ancilla registers next to each other to illustrate the `Evo` gate in Fig. 12. We first employ a quantum multiplier, where extra ancilla qubits (highlighted in red) are introduced to record the result, to compute the product $N_A N_B$ of two boxes A and B . Then, we use the phase gates in Eq. (12) to generate the phases, and finally uncompute the multiplier, which is realized by its inverse gate. All pairs of ancilla registers on which `Evo` is applied are determined by the interaction list of each box, as detailed in Sec. II A. The compute phase terminates upon completing the level that contains four boxes on a 1D lattice.

The final step is to execute the uncompute phase, which transfers the phase back to the qubits representing the quantum state. As discussed in Sec. II B, this is achieved by applying the inverses of the quantum arithmetic circuits in the reverse order. Since the multipliers have already been uncomputed in this example, it suffices to apply the inverses of the quantum adders, as shown in Fig. 13.

Appendix C: Grid discretization for ab initio molecular Hamiltonians

R. White et al. have proposed a local real-space Gausslet basis set discretization with applications to quantum chemistry, with a favorable trade-off between sparsity and smoothness [86–88]. Here, we illustrate how to apply a grid discretization to the following real-space representation of a molecular Hamiltonian (within the Born-Oppenheimer approximation):

$$H = T + V = \sum_{\sigma} \int d\mathbf{r} \hat{\psi}_{\mathbf{r}\sigma}^\dagger \left(-\frac{1}{2} \nabla^2 + v(\mathbf{r}) \right) \hat{\psi}_{\mathbf{r}\sigma} + \frac{1}{2} \sum_{\sigma, \sigma'} \int d\mathbf{r} d\mathbf{r}' \hat{\psi}_{\mathbf{r}\sigma}^\dagger \hat{\psi}_{\mathbf{r}'\sigma'}^\dagger \frac{1}{|\mathbf{r} - \mathbf{r}'|} \hat{\psi}_{\mathbf{r}'\sigma'} \hat{\psi}_{\mathbf{r}\sigma}, \quad (\text{C1})$$

where $\hat{\psi}_{\mathbf{r}\sigma}$ and $\hat{\psi}_{\mathbf{r}\sigma}^\dagger$ are annihilation and creation operator for spin σ at position \mathbf{r} , respectively. Employing the grid approximation, we replace the operator $\hat{\psi}_{\mathbf{r}\sigma}$ with grid

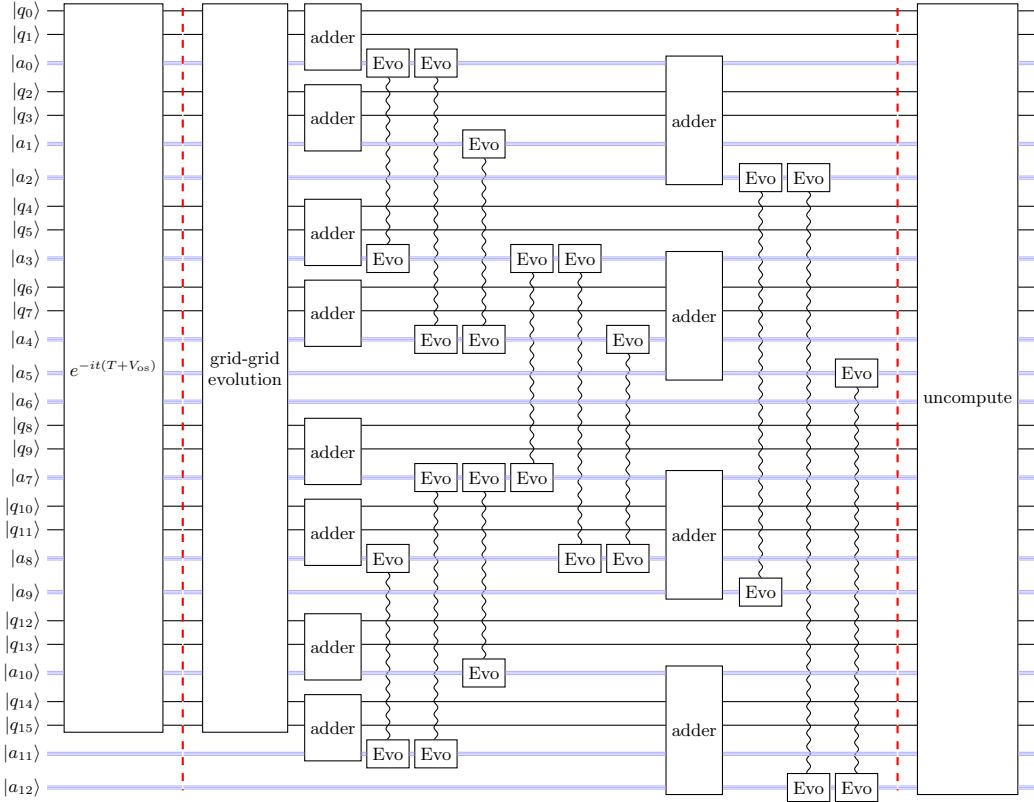


Figure 11: The overall quantum circuit implementing the 0th-order Q2FMM, instantiated for a 1D lattice (see Fig. 10) for visual clarity. The qubits corresponding to physical sites are labeled by $|q_i\rangle$, while the ancilla registers are labeled by $|a_i\rangle$ and represented by blue bundle lines. The kinetic and on-site time evolution operator $e^{-it(T+V_{\text{os}})}$ and the so-called grid-grid evolution only act on physical sites but not on the ancilla registers. The **Evo** gates acting on different boxes can be executed in parallel (but are displayed sequentially in this circuit diagram).

annihilation operators:

$$\hat{\psi}_{\mathbf{r}\sigma} \rightarrow \sum_{i=1}^N \delta(\mathbf{r} - \mathbf{r}_i) \hat{a}_{i\sigma} \quad (\text{C2})$$

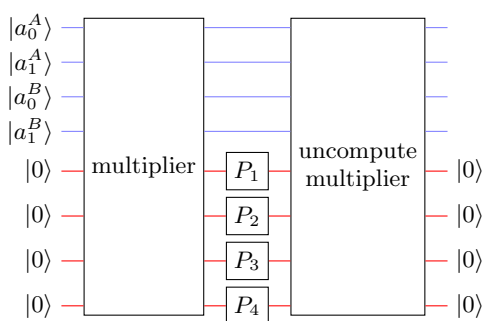


Figure 12: An example of the *Evo* gate applied to the ancilla registers $|a^A\rangle$ and $|a^B\rangle$ corresponding to boxes A and B , respectively. The additional ancilla qubits (red) are immediately discarded in a 2D neutral atom quantum computer after use, since uncomputing the quantum multiplier resets them to the $|0\rangle$ state. For this reason, they are not drawn in Fig. 11.

where $\hat{a}_{i\sigma}$ is the annihilation operator for grid point i , r_i is the position of grid point i , and N is the total number of grid points. Inserting Eq. (C2) into the Hamiltonian Eq. (C1), the Coulomb term V can be re-written as:

$$V = \frac{1}{2} \sum_{i \neq j} \frac{1}{|\mathbf{r}_i - \mathbf{r}_u|} \hat{n}_i \hat{n}_u, \quad (C3)$$

which only contains the grid-grid Coulomb interaction. The kinetic term T only contains nearest-neighbor hopping terms by replacing ∇^2 by finite difference approximations.

The difficulty in simulating Eq. (C3) using Q2FMM lies in the need for a three-dimensional grid setting to capture the electron's motion in three-dimensional space. For plane- or chain-structured molecules, electrons move freely in the first two dimensions, but their motion in the third dimension is highly confined. In such cases, it is feasible to map the three-dimensional lattice onto a two-dimensional quantum device. However, simulating general molecules with fully three-dimensional geometries still requires a quantum device with a genuine three-dimensional structure or all-to-all connectivity.

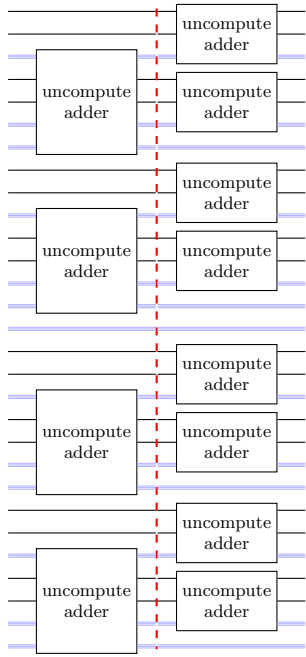


Figure 13: Applied in reverse order, the uncompute procedure first “splits” the largest boxes, as also illustrated in Fig. 5, and continues until the finest level is reached.

[1] R. P. Feynman, Simulating physics with computers, *International Journal of Theoretical Physics* **21**, 467 (1982).

[2] S. Lloyd, Universal quantum simulators, *Science* **273**, 1073 (1996).

[3] S. McArdle, S. Endo, A. Aspuru-Guzik, S. C. Benjamin, and X. Yuan, Quantum computational chemistry, *Reviews of Modern Physics* **92**, 015003 (2020).

[4] I. M. Georgescu, S. Ashhab, and F. Nori, Quantum simulation, *Reviews of Modern Physics* **86**, 153 (2014).

[5] M. Reiher, N. Wiebe, K. M. Svore, D. Wecker, and M. Troyer, Elucidating reaction mechanisms on quantum computers, *Proc. Natl. Acad. Sci. U.S.A.* **114**, 7555 (2017).

[6] F. Arute, K. Arya, R. Babbush, D. Bacon, J. C. Bardin, R. Barends, S. Boixo, M. Broughton, B. B. Buckley, D. A. Buell, and et al., Hartree-fock on a superconducting qubit quantum computer, *Science* **369**, 1084 (2020).

[7] J. Preskill, Quantum computing in the nisq era and beyond, *Quantum* **2**, 79 (2018).

[8] L. Lin and Y. Tong, Heisenberg-limited ground-state energy estimation for early fault-tolerant quantum computers, *PRX Quantum* **3**, 010318 (2022).

[9] C. Monroe, W. C. Campbell, L.-M. Duan, Z.-X. Gong, A. V. Gorshkov, P. W. Hess, R. Islam, K. Kim, N. M. Linke, G. Pagano, and et al., Programmable quantum simulations of spin systems with trapped ions, *Rev. Mod. Phys.* **93**, 025001 (2021).

[10] J. Hubbard, Electron correlations in narrow energy bands, *Proceedings of the Royal Society of London. Series A. Mathematical and Physical Sciences* **276**, 238 (1963).

[11] D. P. Arovas, E. Berg, S. A. Kivelson, and S. Raghu, The hubbard model, *Annual Review of Condensed Matter Physics* **13**, 239 (2022).

[12] D. J. Scalapino, A common thread: The pairing interaction for unconventional superconductors, *Reviews of Modern Physics* **84**, 1383 (2012).

[13] M. Imada, A. Fujimori, and Y. Tokura, Metal-insulator transitions, *Reviews of Modern Physics* **70**, 1039 (1998).

[14] P. A. Lee, N. Nagaosa, and X.-G. Wen, Doping a mott insulator: Physics of high-temperature superconductivity, *Reviews of Modern Physics* **78**, 17 (2006).

[15] R. Pariser and R. G. Parr, A semi-empirical theory of the electronic spectra and electronic structure of complex unsaturated molecules. ii, *The Journal of Chemical Physics* **21**, 767 (1953).

[16] J. A. Pople, Electron interaction in unsaturated hydrocarbons, *Transactions of the Faraday Society* **49**, 1375 (1953).

[17] A. J. Heeger, S. Kivelson, J. R. Schrieffer, and W.-P. Su, Solitons in conducting polymers, *Reviews of Modern Physics* **60**, 781 (1988).

[18] F. Verstraete and J. I. Cirac, Mapping local hamiltonians of fermions to local hamiltonians of spins, *J. Stat. Mech. Theory Exp.* **10.1088/1742-5468/2005/09/P09012** (2005).

[19] S. B. Bravyi and A. Y. Kitaev, Fermionic quantum computation, *Ann. Phys.* **298**, 210 (2002).

[20] C. Derby, J. Klassen, J. Bausch, and T. Cubitt, Compact fermion to qubit mappings, *Phys. Rev. B* **104**, 035118 (2021).

[21] L. Clinton, J. Bausch, and T. Cubitt, Hamiltonian simulation algorithms for near-term quantum hardware, *Nat. Commun.* **12**, 4989 (2021).

[22] I. D. Kivlichan, J. R. McClean, N. Wiebe, C. Gidney, A. Aspuru-Guzik, G. K.-L. Chan, and R. Babbush, Quantum simulation of electronic structure with linear depth and connectivity, *Phys. Rev. Lett.* **120**, 110501 (2018).

[23] M. C. Tran, A. Ehrenberg, A. Y. Guo, P. Titum, D. A. Abanin, A. V. Gorshkov, and A. Deshpande, Locality and digital quantum simulation of power-law interactions, *Phys. Rev. X* **10**, 031009 (2020).

[24] A. M. Childs, Y. Su, M. C. Tran, N. Wiebe, and S. Zhu, Theory of trotter error with commutator scaling, *Physical Review X* **11**, 011020 (2021).

[25] J. Barnes and P. Hut, A hierarchical $\mathcal{O}(n \log n)$ force-calculation algorithm, *Nature* **324**, 446 (1986).

[26] L. Ying, A pedestrian introduction to fast multipole methods, *Sci. China Math.* **55**, 1043 (2012).

[27] L. Greengard and V. Rokhlin, A fast algorithm for particle simulations, *J. Comput. Phys.* **73**, 325 (1987).

[28] E. Darve, The fast multipole method: Numerical implementation, *J. Comput. Phys.* **160**, 195 (2000).

[29] S. Wang, X. Li, W. J. B. Lee, S. Deb, E. Lim, and A. Chattopadhyay, A comprehensive study of quantum arithmetic circuits, *Philosophical Transactions A* **383**, 20230392 (2025).

[30] T. G. Draper, S. A. Kutin, E. M. Rains, and K. M. Svore, A logarithmic-depth quantum carry-lookahead adder, *Quantum Inf. Comput.* **6**, 351 (2006).

[31] Y. Takahashi, S. Tani, and N. Kunihiro, Quantum addition circuits and unbounded fan-out, *Quantum Inf. Comput.* **10**, 872 (2010).

[32] T. G. Draper, Addition on a quantum computer, arXiv preprint quant-ph/0008033 [10.48550/arXiv.quant-ph/0008033](https://arxiv.org/abs/10.48550/arXiv.quant-ph/0008033) (2000).

[33] M. Remaud and V. Vandeale, Ancilla-free quantum adder with sublinear depth, in *International Conference on Reversible Computation* (Springer, 2025) pp. 137–154.

[34] S. Dutta, D. Bhattacharjee, and A. Chattopadhyay, Quantum circuits for toom-cook multiplication, *Phys. Rev. A* **98**, 012311 (2018).

[35] S. Kepley and R. Steinwandt, Quantum circuits for \mathbb{F}_{2^n} -multiplication with subquadratic gate count, *Quantum Information Processing* **14**, 2373 (2015).

[36] F. Orts, E. Filatovas, G. Ortega, J. SanJuan-Estrada, and E. Garzón, Improving the number of t gates and their spread in integer multipliers on quantum computing, *Phys. Rev. A* **107**, 042621 (2023).

[37] P. Høyer and R. Špalek, Quantum fan-out is powerful, *Theory of Computing* **1**, 81 (2005).

[38] S. Hollerith, K. Srakaew, D. Wei, A. Rubio-Abadal, D. Adler, P. Weckesser, A. Kruckenhauser, V. Walther, R. van Bijnen, J. Rui, and et al., Realizing distance-selective interactions in a rydberg-dressed atom array, *Phys. Rev. Lett.* **128**, 113602 (2022).

[39] R. Tao, M. Ammenwerth, F. Gyger, I. Bloch, and J. Zeiher, High-fidelity detection of large-scale atom arrays in an optical lattice, *Phys. Rev. Lett.* **133**, 013401 (2024).

[40] D. Wei, D. Adler, K. Srakaew, S. Agrawal, P. Weckesser, I. Bloch, and J. Zeiher, Observation of brane parity or- der in programmable optical lattices, *Phys. Rev. X* **13**, 021042 (2023).

[41] T. M. Graham, Y. Song, J. Scott, C. Poole, L. Phutti-tarn, K. Jooja, P. Eichler, X. Jiang, A. Marra, B. Grinke-meyer, and et al., Multi-qubit entanglement and algorithms on a neutral-atom quantum computer, *Nature* **604**, 457 (2022).

[42] S. J. Evered, D. Bluvstein, M. Kalinowski, S. Ebadi, T. Manovitz, H. Zhou, S. H. Li, A. A. Geim, T. T. Wang, N. Maskara, and et al., High-fidelity parallel entangling gates on a neutral-atom quantum computer, *Nature* **622**, 268 (2023).

[43] D. Bluvstein, H. Levine, G. Semeghini, T. T. Wang, S. Ebadi, M. Kalinowski, A. Keesling, N. Maskara, H. Pichler, M. Greiner, and et al., A quantum processor based on coherent transport of entangled atom arrays, *Nature* **604**, 451 (2022).

[44] L. Schmid, D. F. Locher, M. Rispler, S. Blatt, J. Zeiher, M. Müller, and R. Wille, Computational capabilities and compiler development for neutral atom quantum processors—connecting tool developers and hardware experts, *Quantum Science and Technology* **9**, 033001 (2024).

[45] D. Bluvstein, S. J. Evered, A. A. Geim, S. H. Li, H. Zhou, T. Manovitz, S. Ebadi, M. Cain, M. Kalinowski, D. Hangleiter, and et al., Logical quantum processor based on reconfigurable atom arrays, *Nature* **626**, 58 (2024).

[46] S. J. Evered, M. Kalinowski, A. A. Geim, T. Manovitz, D. Bluvstein, S. H. Li, N. Maskara, H. Zhou, S. Ebadi, M. Xu, and et al., Probing the kitaev honeycomb model on a neutral-atom quantum computer, *Nature* **645**, 341 (2025).

[47] H. J. Manetsch, G. Nomura, E. Bataille, X. Lv, K. H. Leung, and M. Endres, A tweezer array with 6100 highly coherent atomic qubits, *Nature* **647**, 60 (2025).

[48] N.-C. Chiu, E. C. Trapp, J. Guo, M. H. Abobeih, L. M. Stewart, S. Hollerith, P. L. Stroganov, M. Kalinowski, A. A. Geim, S. J. Evered, and et al., Continuous operation of a coherent 3,000-qubit system, *Nature* **646**, 1075 (2025).

[49] M. Xu, L. H. Kendrick, A. Kale, Y. Gang, C. Feng, S. Zhang, A. W. Young, M. Lebrat, and M. Greiner, A neutral-atom hubbard quantum simulator in the cryogenic regime, *Nature* **642**, 909 (2025).

[50] L. Greengard and J. Huang, A new version of the fast multipole method for screened coulomb interactions in three dimensions, *Journal of Computational Physics* **180**, 642 (2002).

[51] H. Cheng, W. Y. Crutchfield, Z. Gimbutas, L. Greengard, J. Ethridge, J. Huang, and V. Rokhlin, A wide-band fast multipole method for the helmholtz equation in three dimensions, *Journal of Computational Physics* **216**, 300 (2006).

[52] B. Engquist and L. Ying, Fast directional multilevel algorithms for oscillatory kernels, *SIAM Journal on Scientific Computing* **29**, 1710 (2007).

[53] W. C. Chew, J.-M. Jin, E. Michielssen, and J. Song, eds., *Fast and Efficient Algorithms in Computational Electromagnetics* (Artech House, Boston and London, 2001).

[54] A.-K. Tornberg and L. Greengard, A fast multipole method for the three-dimensional stokes equations, *Journal of Computational Physics* **227**, 1613 (2008).

[55] Y. Liu, *Fast Multipole Boundary Element Method: The-*

ory and Applications in Engineering (Cambridge University Press, 2009).

[56] Z. Gimbutas and L. Greengard, A fast multipole method for the evaluation of elastostatic fields in a half-space with zero normal stress, *Advances in Computational Mathematics* **42**, 1293 (2016).

[57] N. A. Gumerov and R. Duraiswami, Fast multipole method for the biharmonic equation in three dimensions, *Journal of Computational Physics* **215**, 363 (2006).

[58] L. Ying, G. Biros, and D. Zorin, A kernel-independent adaptive fast multipole algorithm in two and three dimensions, *Journal of Computational Physics* **196**, 591 (2004).

[59] T. Helgaker, P. Jørgensen, and J. Olsen, *Molecular Electronic-Structure Theory* (Wiley, Chichester, 2000).

[60] A. J. Stone, *The Theory of Intermolecular Forces*, 2nd ed. (Oxford University Press, Oxford, 2013).

[61] D. M. Brink and G. R. Satchler, *Angular Momentum*, 2nd ed. (Clarendon Press, Oxford, 1968).

[62] H. F. Trotter, On the product of semi-groups of operators, *Proceedings of the American Mathematical Society* **10**, 545 (1959).

[63] M. Suzuki, Generalized trotter's formula and systematic approximants of exponential operators and inner derivations with applications to many-body problems, *Communications in Mathematical Physics* **51**, 183 (1976).

[64] D. W. Berry, G. Ahokas, R. Cleve, and B. C. Sanders, Efficient quantum algorithms for simulating sparse hamiltonians, *Communications in Mathematical Physics* **270**, 359 (2007).

[65] A. M. Childs and Y. Su, Nearly optimal lattice simulation by product formulas, *Physical Review Letters* **123**, 050503 (2019).

[66] G. D. Kahanamoku-Meyer and N. Y. Yao, Fast quantum integer multiplication with zero ancillas, arXiv preprint arXiv:2403.18006 [10.48550/arXiv.2403.18006](https://arxiv.org/abs/2403.18006) (2024).

[67] M. A. Nielsen and I. L. Chuang, *Quantum Computation and Quantum Information: 10th Anniversary Edition* (Cambridge University Press, 2011).

[68] D. Gottesman, *An introduction to quantum error correction and fault-tolerant quantum computation* (2009), arXiv:0904.2557.

[69] K. Sahay, Y. Lin, S. Huang, K. R. Brown, and S. Puri, Error correction of transversal cnot gates for scalable surface-code computation, *PRX Quantum* **6**, 020326 (2025).

[70] F. D. Chiara, M. Nibbi, Y. Shen, and R. V. Beeumen, Efficient lcu block encodings through dicke states preparation (2025), arXiv:2507.20887.

[71] D. Kielpinski, C. Monroe, and D. J. Wineland, Architecture for a large-scale ion-trap quantum computer, *Nature* **417**, 709 (2002).

[72] R. B. Blakestad, C. Ospelkaus, A. P. VanDevender, J. M. Amini, J. Britton, D. Leibfried, and D. J. Wineland, High-fidelity transport of trapped-ion qubits through an x-junction trap array, *Phys. Rev. Lett.* **102**, 153002 (2009).

[73] D. Schoenberger, S. Hillmich, M. Brandl, and R. Wille, Shuttling for scalable trapped-ion quantum computers, *IEEE Trans. Comput.-Aided Des. Integr. Circuits Syst.* **44**, 2144 (2025).

[74] J. M. Pino, J. M. Dreiling, C. Figgatt, J. P. Gaebler, S. A. Moses, M. S. Allman, C. H. Baldwin, M. Foss-Feig, D. Hayes, K. Mayer, and et al., Demonstration of the trapped-ion quantum ccd computer architecture, *Nature* **592**, 209 (2021).

[75] S. A. Moses, C. H. Baldwin, M. S. Allman, R. Ancona, L. Ascarrunz, C. Barnes, J. P. Bartolotta, B. Bjork, P. Blanchard, M. Bohn, and et al., A race-track trapped-ion quantum processor, *Phys. Rev. X* **13**, 041052 (2023).

[76] S.-A. Guo, Y.-K. Wu, J. Ye, L. Zhang, W.-Q. Lian, R. Yao, Y. Wang, R.-Y. Yan, Y.-J. Yi, Y.-L. Xu, and et al., A site-resolved two-dimensional quantum simulator with hundreds of trapped ions, *Nature* **630**, 613 (2024).

[77] B.-W. Li, Y.-K. Wu, Q.-X. Mei, R. Yao, W.-Q. Lian, M.-L. Cai, Y. Wang, B.-X. Qi, L. Yao, L. He, and et al., Probing critical behavior of long-range transverse-field ising model through quantum kibble-zurek mechanism, *PRX Quantum* **4**, 010302 (2023).

[78] M. Khazali and K. Mølmer, Fast multiqubit gates by adiabatic evolution in interacting excited-state manifolds of rydberg atoms and superconducting circuits, *Physical Review X* **10**, 021054 (2020).

[79] J. T. Young, P. Bienias, R. Belyansky, A. M. Kaufman, and A. V. Gorshkov, Asymmetric blockade and multi-qubit gates via dipole-dipole interactions, *Physical Review Letters* **127**, 120501 (2021).

[80] Y. Song, L. Beltrán, I. Besedin, M. Kerschbaum, M. Pechal, F. Swiadek, C. Hellings, D. C. Zanuz, A. Flasby, J.-C. Besse, and A. Wallraff, Realization of constant-depth fan-out with real-time feedforward on a superconducting quantum processor, *Phys. Rev. Applied* **24**, 024068 (2025).

[81] E. Bäumer and S. Woerner, Measurement-based long-range entangling gates in constant depth, *Phys. Rev. Res.* **7**, 023120 (2025).

[82] L. Ruiz-Perez and J. C. Garcia-Escartin, Quantum arithmetic with the quantum fourier transform, *Quantum Inf. Process.* **16**, 152 (2017).

[83] D. W. Berry, K. Wan, A. D. Baczewski, E. C. Eklund, A. Tikku, and R. Babbush, *Quantum simulation of chemistry via quantum fast multipole method* (2025), arXiv:2510.07380.

[84] A. Kay, Tutorial on the quantikz package (2018), arXiv:1809.03842.

[85] B. Desef, Yquant: Typesetting quantum circuits in a human-readable language (2020), arXiv:2007.12931.

[86] S. R. White, Hybrid grid/basis set discretizations of the schrödinger equation, *J. Chem. Phys.* **147**, 244102 (2017).

[87] E. M. Stoudenmire and S. R. White, Sliced basis density matrix renormalization group for electronic structure, *Phys. Rev. Lett.* **119**, 046401 (2017).

[88] S. R. White and E. M. Stoudenmire, Multisliced gaus-slet basis sets for electronic structure, *Phys. Rev. B* **99**, 081110(R) (2019).